Article

Quantum-amplified global-phase spectroscopy on an optical clock transition

https://doi.org/10.1038/s41586-025-09578-8

Received: 1 April 2025

Accepted: 27 August 2025

Published online: 8 October 2025

Check for updates

Leon Zaporski[1,5], Qi Liu[1,5], Gustavo Velez[1,5], Matthew Radzihovsky[1,5], Zeyang Li[1,2], Simone Colombo[1,3], Edwin Pedrozo-Peñafiel[1,4] & Vladan Vuletić[1]✉

Optical lattice clocks are at the forefront of precision metrology[1–6], operating near a standard quantum limit set by quantum noise[4,7]. Harnessing quantum entanglement offers a promising route to surpass this limit[8–15]; however, there are practical difficulties in terms of scalability and measurement resolution requirements[16,17]. Here we adapt the holonomic quantum gate concept[18] to develop a new Rabi-type 'global-phase spectroscopy' that uses the detuning-sensitive global Aharonov–Anandan phase[19]. With this approach, we can demonstrate quantum-amplified time-reversal spectroscopy on an optical clock transition that achieves directly measured 2.4(7) dB metrological gain and 4.0(8) dB improvement in laser noise sensitivity beyond the standard quantum limit. To this end, we introduce rotary echo to protect the dynamics from inhomogeneities in light–atom coupling and implement a laser-noise-cancelling differential measurement through symmetric phase encoding in two nuclear spin states. Our technique is not limited by measurement resolution, scales easily because of the global nature of entangling interaction and exhibits high resilience to typical experimental imperfections. We expect it to be broadly applicable to next-generation atomic clocks and other quantum sensors approaching the fundamental quantum precision limits[20–22].

The progress of science is largely determined by the level of measurement sensitivity to increasingly weaker signals. Among the most precise sensors in the world, optical lattice clocks have achieved unprecedented fractional frequency instability and inaccuracy at the 10^{-18} level[1–6]. Apart from serving as precise time references, optical lattice clocks have several applications in advancing relativistic geodesy[23], detecting variations of fundamental constants[24] and gravitational waves[25], testing Lorentz invariance[26] and searching for dark matter[27].

The short-term stability of optical clocks is guaranteed by locking clock lasers to ultrastable cavity references, whereas the cancellation of long-term laser frequency drift entails closed-loop stabilization to the atomic clock transition. Here, the relative phase between laser and atoms due to a detuning from atomic resonance is converted into a population imbalance that can be directly measured. The accuracy and stability of the clock are conditioned by the precision with which this phase can be estimated. For an ensemble of N independent atoms, the single-shot uncertainty in phase estimation is fundamentally limited by quantum projection noise, $\Delta\phi = 1/\sqrt{N}$, known as the standard quantum limit (SQL)[8]. State-of-the-art optical lattice clocks have reached this limit after suppressing the Dick noise, either by shortening dead time[4] or by using synchronous differential comparisons in multiplexed clocks[7]. By harnessing multi-particle entanglement, this precision cap can be further lowered to the Heisenberg limit of $\delta\phi = 1/N$, which is the ultimate sensitivity allowed by quantum mechanics[8]. Highly entangled resources, such as Greenberger–Horne–Zeilinger (GHZ) states, have been prepared and have approached this limit in small-scale systems[28–30] and were very recently leveraged in optical lattice clocks to achieve sub-SQL frequency instability[12]. However, GHZ states are difficult to prepare and maintain for large atomic numbers.

Squeezed states[13–15] are another widely explored class of entangled states. They feature wider dynamic range and higher tolerance to decoherence and loss compared with GHZ states, at the expense of intermediate levels of improvement beyond the SQL. Till now, spin squeezing has been generated in microwave-coupled manifolds[31–34], in momentum space[35,36] and on optical transitions[22,37], on which it survived well beyond tens of milliseconds (ref. 37). Spin squeezing has applications in atomic magnetometers[38,39], gravimeters[40] and clocks[37,41,42]. Spin-squeezed states can be detected either directly, which requires measurement resolution below the quantum projection noise limit, or by further manipulation of the entangled state after phase accumulation, also known as interaction-based readout[43]. The latter includes quantum phase amplification techniques[44–47], typically based on time-reversed squeezing dynamics, which can be used to approach the Heisenberg limit without single-particle resolution[16,17]. Extensions of the interaction-based readout emerged from variational optimization of Ramsey interferometry[20,21] to balance local sensitivity and dynamic range while minimizing the frequency Allan deviation and were recently

[1]MIT-Harvard Center for Ultracold Atoms and Research Laboratory of Electronics, Massachusetts Institute of Technology, Cambridge, MA, USA. [2]Department of Applied Physics, Stanford University, Stanford, CA, USA. [3]Department of Physics, University of Connecticut, Storrs, CT, USA. [4]Department of Physics, University of Florida, Gainesville, FL, USA. [5]These authors contributed equally: Leon Zaporski, Qi Liu, Gustavo Velez, Matthew Radzihovsky. ✉e-mail: vuletic@mit.edu

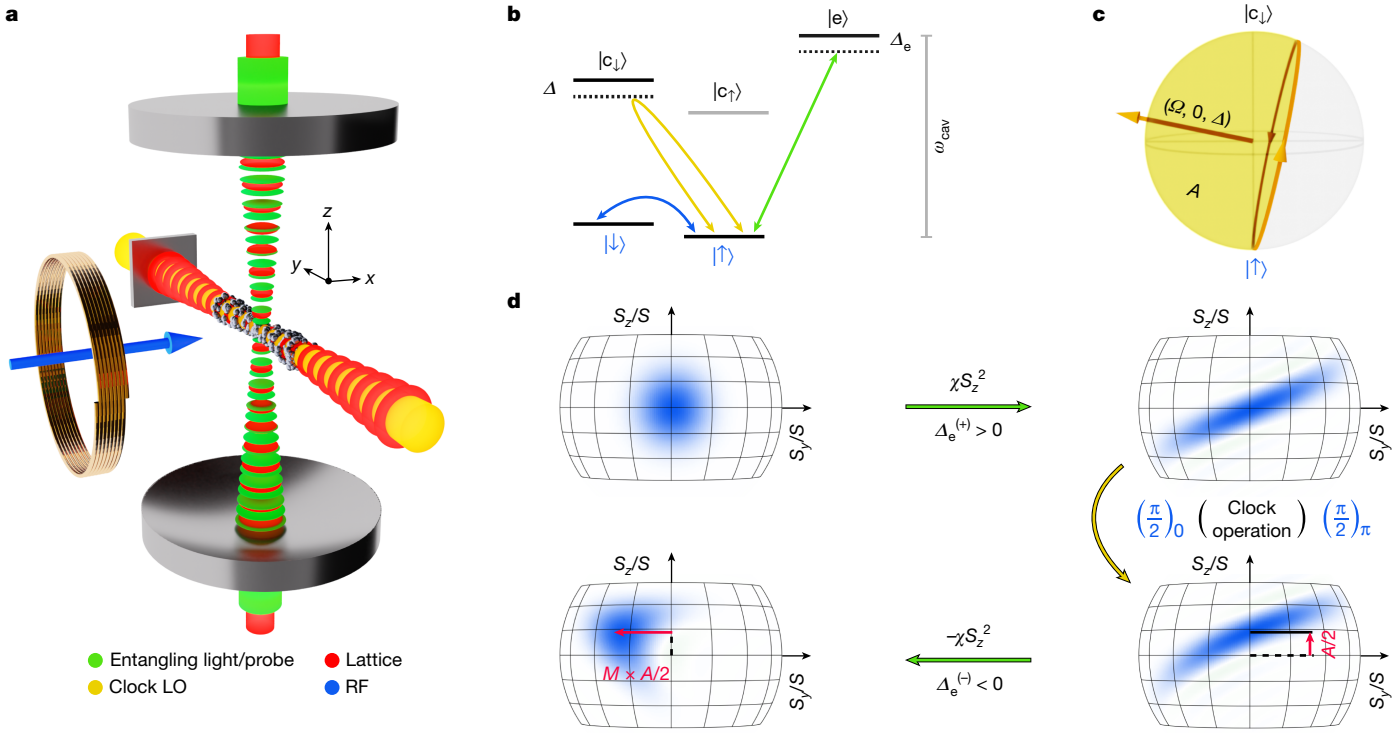

Fig. 1 | Experimental setup for entangled time-reversal GPS. a, Laser-cooled atoms are confined in a two-dimensional optical lattice (red) inside a high-finesse optical cavity. A transverse lattice along the *y* axis is created by retro-reflection off the (square) mirror. Squeezing and probing light (green) is sent through the cavity along the *z* axis, while the clock laser (yellow) is aligned with the transverse lattice. The blue arrow represents the RF field used for rotations of the nuclear Zeeman ground states $\{|\uparrow\rangle, |\downarrow\rangle\}$. The objects in the picture are rendered not to scale. **b**, Simplified energy-level diagram with states $|\downarrow\rangle \equiv |^1S_0, m_I = -\frac{1}{2}\rangle$, $|\uparrow\rangle \equiv |^1S_0, m_I = +\frac{1}{2}\rangle$, $|c_\downarrow\rangle \equiv |^3P_0, m_I = -\frac{1}{2}\rangle$, $|c_\uparrow\rangle \equiv |^3P_0, m_I = +\frac{1}{2}\rangle$ and $|e\rangle \equiv |^3P_1, m_F = +\frac{3}{2}\rangle$, quantized along the *z* axis from **a**. The arrows represent the three control fields from **a**. The cavity mode (vertical grey line) is tuned on resonance with the $|\uparrow\rangle \rightarrow |e\rangle$ transition. **c**, In GPS, the clock laser drives the optical qubit state along the closed trajectory (yellow curve) on the unit-radius Bloch sphere, encoding a geometric Aharonov–Anandan phase, which equals half of the enclosed area, $A/2$, after a single cyclic evolution. The area A depends on the clock LO detuning, providing a method to measure LO frequency while operating nominally on atomic resonance. **d**, Illustration of quantum amplification based on time reversal. The initial CSS is squeezed by a green laser pulse and rotated by π/2 by an RF pulse before the clock LO pulse is applied to induce a shift of $A/2$ that is mapped back onto the S_z axis by another π/2 RF pulse. Unsqueezing $-\chi S_z^2$ subsequently amplifies the signal to $M \times A/2$ along the S_y axis (with M constant and independent of A in the vicinity of $A = 0$ and $A = 2\pi$). The blue shading on the generalized Bloch spheres illustrates the Wigner quasi-probability distributions in the ground-state manifold, $\{|\uparrow\rangle, |\downarrow\rangle\}^{\otimes N}$.

demonstrated on an optical transition in trapped ions[22]. Despite its potential significance for optical lattice clocks, the interaction-based readout on an optical clock transition in a neutral-atom system has not been demonstrated so far.

Here we report the experimental quantum amplification of an optical clock phase in a neutral-atom ensemble and demonstrate spectroscopic precision enhancement of 2.4(7) dB beyond the SQL. This is achieved through cavity-mediated one-axis twisting (OAT)[48], which generates squeezing and unsqueezing dynamics in the nuclear ground states of laser-cooled ^{171}Yb atoms[49]. To mitigate fast phase diffusion on the optical transition due to high-frequency noise of the local oscillator (LO) laser[50], we develop a method that replaces conventional Ramsey spectroscopy with a new Rabi-type 'global-phase spectroscopy' (GPS) that relies on driven cyclic evolution. In this approach, the driven optical qubit acquires a global Aharonov–Anandan phase[19], which realizes a detuning-sensitive holonomic quantum phase gate[18] between the ground states. This GPS method allows us to extend the entanglement enhancement techniques to Rabi-type spectroscopy. While it retains the same d.c. sensitivity to the LO laser noise as conventional Rabi spectroscopy, the GPS features reduced sensitivity to high-frequency phase (frequency) noise, following $\propto f^{-4}$ ($\propto f^{-6}$) scaling. This is substantially lower than that of Rabi spectroscopy, $\propto f^{-2}$ ($\propto f^{-4}$), and Ramsey spectroscopy, $\propto f^{0}$ ($\propto f^{-2}$) (Supplementary Information). Furthermore, while conventional Rabi spectroscopy measures population imbalance, which necessitates side-of-fringe operation, GPS measures phase and exhibits maximal sensitivity on resonance—an optimal condition for feedback. This fact allows us to also integrate GPS with a resonant rotary echo[51], which refocuses the inhomogeneities in light–atom coupling[52] and facilitates implementation of composite pulse sequences.

To characterize the metrological gain available to stabilize a noisy LO laser, we leverage the multi-level structure of ^{171}Yb by performing a differential measurement on two clock transitions in a single ensemble. The differential phase imprinted on a squeezed probe state is amplified by a time-reversal protocol[16,44,47], leading to a metrological gain of 2.4(7) dB below the SQL (4.0(8) dB when subtracting the residual laser noise), one of the first such demonstrations in a scalable neutral-atom system with global entangling interactions.

Our experiments are performed with an ensemble of $N = 2.2(4) \times 10^2$ laser-cooled ^{171}Yb atoms that are trapped in a two-dimensional optical lattice inside a high-finesse optical cavity (Fig. 1a). We initialize the atoms in the $|\uparrow\rangle \equiv |^1S_0, m_I = +\frac{1}{2}\rangle$ state and rotate them into a coherent superposition of $|\uparrow\rangle$ and $|\downarrow\rangle \equiv |^1S_0, m_I = -\frac{1}{2}\rangle$ states with a resonant radiofrequency (RF) driving field. Optical phase encoding involves back-and-forth transfer of the $|\uparrow\rangle$ state or $|\downarrow\rangle$ state to one of the $\{|c_\uparrow\rangle \equiv |^3P_0, m_I = +\frac{1}{2}\rangle, |c_\downarrow\rangle \equiv |^3P_0, m_I = -\frac{1}{2}\rangle\}$ clock states (Fig. 1b) and is achieved with a clock laser referenced to a commercial rack-mounted ultralow-expansion (ULE) cavity. In this process, a near-resonant Rabi pulse drives the optical qubit state around the $(\Omega, 0, \Delta)$ axis to traverse a closed trajectory on the Bloch sphere (Fig. 1c), in which Ω and Δ are the resonant Rabi frequency and the laser detuning, respectively. The state of an atom evolves according to

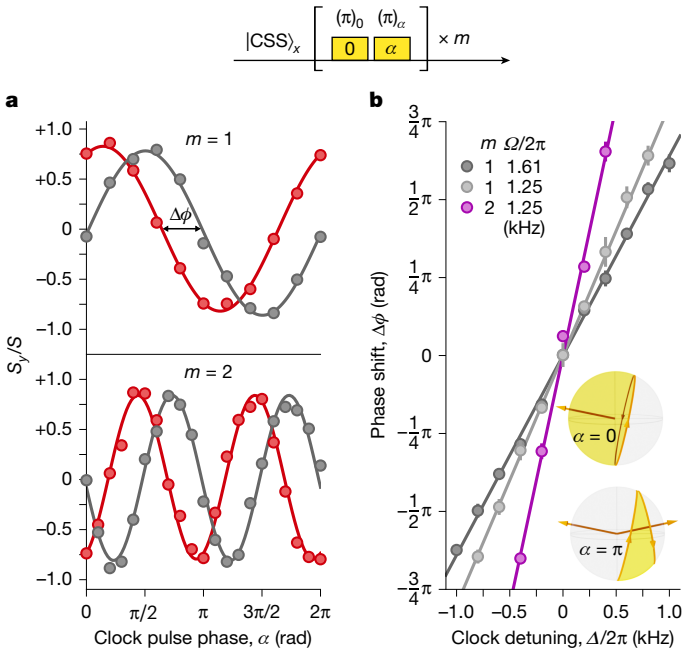

Fig. 2 | Optical global phase encoding and readout. a, A geometric phase is imprinted onto the $|\uparrow\rangle$ state using strings of m pairs of clock π-pulses with alternating phases, 0 and α, and is mapped onto the normalized collective spin S_y/S. The grey and red points show S_y/S as a function of α for resonant and off-resonant optical driving, respectively. Here, $\Omega/(2\pi) = 4.5$ kHz for all the datasets, as well as $\Delta/(2\pi) = 1$ kHz for $m = 1$ and $\Delta/(2\pi) = 1.2$ kHz for $m = 2$. **b**, Dependence of the phase shift, $\Delta\phi$, on the clock laser detuning for different Rabi frequencies and numbers m of pulse pairs. The lines represent the theoretical prediction $\Delta\phi = \pi m\Delta/\Omega$ for $\Delta/\Omega \ll 1$. Throughout this study, the labels above the pulses in the pulse diagrams, of the form $(\theta)_\varphi$, specify the pulse amplitude (in terms of the resonant rotation angle, θ, expressed in radians) and phase (φ, expressed in radians). Inset, trajectories traversed on the Bloch spheres for off-resonant Rabi pulses for $\alpha = 0$ and $\alpha = \pi$. Error bars indicate 1 s.d.

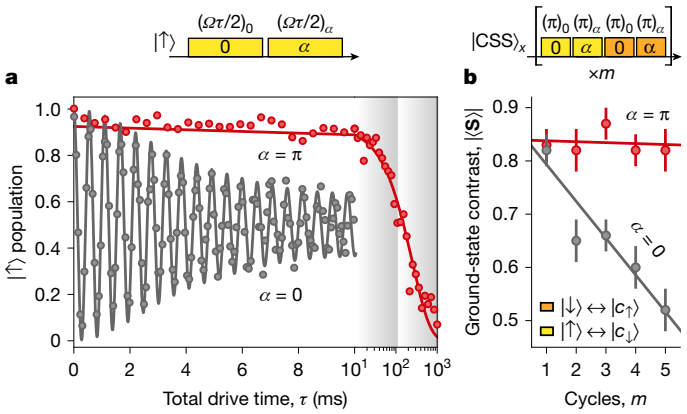

Fig. 3 | Rabi and rotary echo sequences on the clock transition. a, The grey and red points show the $|\uparrow\rangle$ population oscillation under the resonant Rabi ($\alpha = 0$) and rotary echo ($\alpha = \pi$) sequences, respectively, with $\Omega/(2\pi) = 1.8$ kHz. The solid lines represent the models of population dynamics factoring the finite temperature effects and slight beam misalignment in agreement with ref. 52, as well as the exponential decay of the clock state over the lifetime of 0.25(2) s. The grey shading highlights the change of the time-axis scale from linear to logarithmic. **b**, The ground-state contrast measured after m cycles of resonant, symmetric phase encoding with $\Omega/(2\pi) = 3.8$ kHz. The red and grey points correspond to the rotary echo sequence and Rabi sequence, respectively. The solid lines represent linear fits. The rotary echo sequence ($\alpha = \pi$) retains high contrast despite inhomogeneously broadened atom–light coupling. Faster contrast decay of the Rabi sequence (grey points), compared with **a**, is likely due to an increase in misalignment angle (from 3.5 mrad to 7 mrad). Error bars indicate 1 s.d.

$$|\psi(\tau)\rangle = \frac{1}{\sqrt{2}}\left[|\downarrow\rangle + e^{-i\frac{\Delta}{2}\tau}(a_\uparrow(\tau)|\uparrow\rangle + a_{c_\downarrow}(\tau)|c_\downarrow\rangle)\right], \quad (1)$$

and by the end of a single cyclic evolution ($\tau \times \sqrt{\Omega^2 + \Delta^2} = 2\pi$), the coupled ground state $|\uparrow\rangle$ recovers its initial population ($a_{c_\downarrow} \approx 0$), acquiring a detuning-dependent geometric phase

$$\phi = -\pi - \frac{\Delta}{2}\tau = -\pi\left(1 + \frac{\Delta}{\sqrt{\Omega^2 + \Delta^2}}\right), \quad (2)$$

known as the Aharonov–Anandan phase[19], the value of which corresponds to half the area enclosed by the trajectory (Methods). The global phase of the optical qubit $\{|\uparrow\rangle, |c_\downarrow\rangle\}$ thus translates to the relative phase between the $|\uparrow\rangle$ and $|\downarrow\rangle$ states and is mapped with an RF rotation into a population difference between $|\uparrow\rangle$ and $|\downarrow\rangle$, which is measured via the cavity (Methods). Overall, the clock laser detuning from the atomic transition Δ is thus measured by the accumulated global phase ϕ.

The above sequence can be performed with unentangled coherent spin states (CSSs) or with spin-squeezed states. To generate spin squeezing, we adopt the cavity feedback method[49]. In essence, we tune the cavity mode to resonance with the $|\uparrow\rangle \rightarrow |e\rangle \equiv |^3P_1, m_F = +\frac{3}{2}\rangle$ transition and send an off-resonant entangling light pulse through the cavity. The atoms in the $|\uparrow\rangle$ state dispersively shift the cavity resonance, which in turn alters the intra-cavity photon number. This leads to a spin-imbalance-dependent light shift captured by the OAT Hamiltonian[49]:

$$\hat{H} = \chi\hat{S}_z^2. \quad (3)$$

Here, $\hat{S}_z$ is a collective spin operator, summed over the spins of all the atoms and χ denotes the squeezing strength. This all-to-all interaction shears the noise distribution of the initial CSS into that of a spin-squeezed state, as shown by the Wigner quasi-probability distributions in Fig. 1d. To realize a process that is tolerant to detection noise and can work with oversqueezed states, we implement effective time reversal (unsqueezing) by flipping the sign of the entangling light detuning and of the Hamiltonian from equation (3) (ref. 47). The squeezing–unsqueezing sequence converts a small optical phase shift $\Delta\phi$ into a shift along S_z that is amplified into a larger shift along the orthogonal quadrature (S_y), thereby achieving phase sensitivity below the SQL.

We start by benchmarking our GPS method on the optical clock transition. To this end, we initialize the atoms in a CSS polarized along the S_x axis of the ground-state Bloch sphere, $\{|\uparrow\rangle, |\downarrow\rangle\}$, and drive a cyclic evolution between $|\uparrow\rangle$ and $|c_\downarrow\rangle$ using two consecutive π-rotations with relative phase α. In the near-resonant case ($\Delta \ll \Omega$), the $|\uparrow\rangle$ state acquires a geometric phase $\Delta\phi$ given by $\Delta\phi = \alpha + \pi(1 + \Delta/\Omega)$. For $\Delta = 0$ and $\alpha = 0$, this is just the minus sign that a spin-½ consisting of states $\{|\uparrow\rangle, |c_\downarrow\rangle\}$ acquires after a 2π Rabi rotation. The phase $\Delta\phi$ is reflected in the measured normalized spin operator S_y/S, which oscillates as α is varied from 0 to 2π. The top two datasets in Fig. 2a show the dependence of S_y/S on α for both resonant (grey points) and off-resonant (red points) driving, which are related by a phase offset $\Delta\phi$, from which the laser detuning can be inferred. As we vary the laser detuning, we observe a linear relationship of the fitted phase shifts shown in Fig. 2b, in good agreement with the theoretical expectation (solid lines). This linear frequency discriminant is a fundamental ingredient of locking the clock laser to the atoms and can be made steeper by extending the interrogation time either through lowering the Rabi frequency or driving a repeated cyclic evolution with $m > 1$. Extending the sequence to m cycles multiplies the resulting phase and detuning sensitivity by a factor m, as shown by the bottom two datasets in Fig. 2a (for $m = 2$). Our theoretical analysis presented in the Supplementary Information shows that a single-cycle sequence is preferred for d.c. measurements,

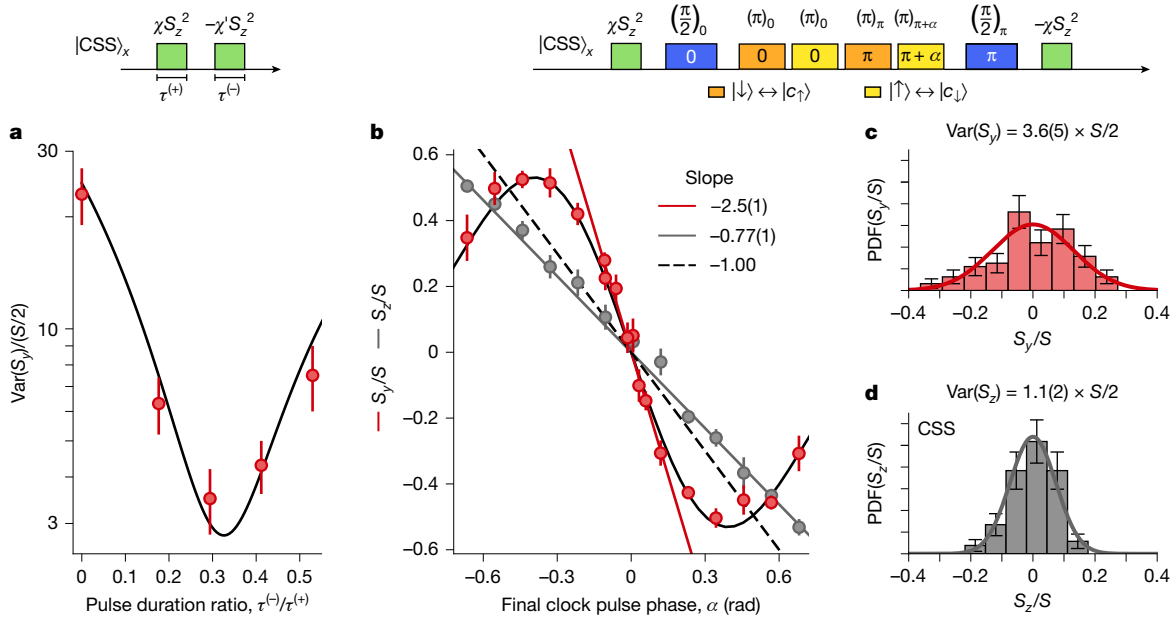

Fig. 4 | Quantum amplification measurement of the optically encoded phase. a, A pair of entangling pulses with durations $\tau^{(\pm)}$ generates the squeezing–unsqueezing dynamics in the ground-state manifold. The red data points show normalized S_y-variances as a function of the pulse duration ratio $\tau^{(-)}/\tau^{(+)}$, with $\tau^{(+)}$ fixed to 8.5 ms, in good agreement with the microscopic model indicated by the black line (Supplementary Information). **b**, The red and grey points represent the average values of S_y/S and S_z/S as a function of the final clock pulse phase in time-reversal and CSS reference differential measurements, respectively. The red and grey lines represent the linear fits of the slope at $\alpha = 0$. The solid black line is a numerical simulation of the data, extending beyond the linear amplification regime. The dashed black line with a negative unity slope represents the signal expected of a perfect CSS reference sequence with no contrast loss. For the equivalent scenario of the clock detuning measurement, α would map to $\pi \times \Delta/\Omega$ (Fig. 2b). **c**, Spin noise measured at $S_y/S = 0$ after a time-reversal sequence. **d**, The CSS reference counterpart of the dataset from **c**. The probability density function (PDF) is estimated based on more than 100 measurement outcomes summarized by the histograms. The colour coding in the pulse diagrams is consistent with Fig. 1a,b (green, entangling light; blue, RF; and yellow/orange, clock laser). Error bars indicate 1 s.d.

whereas a multi-cycle sequence can enhance the a.c. signal sensitivity at particular frequencies.

Single-shot estimation of laser frequency requires maximizing the slope $|dS_y/d\Delta|$ around $\Delta = 0$, which is reached at $\alpha \in \{0, \pi\}$ and $\alpha \in \{0, \pi/2, \pi, 3\pi/2\}$ for sequences with $m = 1$ and $m = 2$, respectively. The $\alpha = 0$ case is simply a Rabi oscillation, whereas the $\alpha = \pi$ case realizes a rotary echo[51], conventionally applied in solid-state spin systems for extending the coherence time of the drive. In our system, rotary echo ensures a better $|\uparrow\rangle$ state population recovery in the presence of inhomogeneous broadening in the atomic cloud, maintaining high signal contrast and enabling near-perfect time reversal.

The effectiveness of the rotary echo sequence in our setup is shown in Fig. 3. We first obtain a simple resonant Rabi sequence benchmark by initializing the system in the $|\uparrow\rangle$ state and driving the atoms through the $|\uparrow\rangle \rightarrow |c_\downarrow\rangle \rightarrow |\uparrow\rangle$ transition. The grey points in Fig. 3a show the optical Rabi oscillation at $\Omega/(2\pi) = 1.8$ kHz, decaying over the timescale of a few milliseconds. This damping can be attributed to the finite temperature of the atomic ensemble, which populates multiple motional states of the transverse lattice, leading to inhomogeneous coupling to the clock laser[52]. The dephasing is remarkably suppressed when using rotary echo. As shown in Fig. 3a (red points), we observe a robust refocusing over hundreds of milliseconds, constrained by the lifetime of the clock state of $T = 0.25(2)$s due to photon scattering from the trapping light.

We now turn to a measurement of the atomic clock phase using GPS. To measure the intrinsic atomic phase stability without being overwhelmed by LO laser noise, we apply our GPS method sequentially on both the $|\uparrow\rangle \rightarrow |c_\downarrow\rangle$ and $|\downarrow\rangle \rightarrow |c_\uparrow\rangle$ transitions, starting from a CSS in the $\{|\uparrow\rangle, |\downarrow\rangle\}$ manifold polarized along the S_x axis (see the pulse sequence above Fig. 3b). We repeat this over multiple cycles for both the Rabi ($\alpha = 0$) and the rotary echo ($\alpha = \pi$) sequences and map the resulting ground-state Bloch vector lengths, $|\langle \mathbf{S} \rangle|$, to display contrast loss. As shown in Fig. 3b, the rotary echo maintains the contrast at the level of about 81% for at least $m = 5$ cycles (red points), proving negligible propagation of the inhomogeneities in light–atom coupling to the geometric phases. In stark comparison, the Rabi sequence features fast contrast decay (grey points). These results indicate that rotary echo GPS can be extended to multi-cycle composite sequences of long total probing times even in the presence of inhomogeneous broadening of the atom–LO coupling.

Equipped with a robust optical phase encoding and detection scheme, we proceed to demonstrate entanglement-enhanced operation of the GPS protocol below the SQL. We set the entangling pulse detunings to $\Delta_e^{(+)}/(2\pi) = 8.33$ MHz and $\Delta_e^{(-)}/(2\pi) = -7.28$ MHz, respectively, for the squeezing and unsqueezing dynamics within the ground-state manifold, $\{|\uparrow\rangle, |\downarrow\rangle\}$ (ref. 47). These parameters were chosen to mitigate the effect of fluctuations in the total atom number, considering the contribution of the $|\downarrow\rangle \rightarrow |^3P_1, m_F = +\frac{1}{2}\rangle$ transition to the OAT dynamics (Supplementary Information).

We prepare a squeezed state whose S_y variance is enlarged by a factor of 23(4) compared with the quantum projection noise of the CSS (Fig. 4a). During the effective time-reversed dynamics, this variance is reduced as we increase the duration $\tau^{(-)}$ of the second (unsqueezing) pulse. We obtain a minimal normalized variance of 3.5(7) for $\tau^{(-)} = 0.29 \times \tau^{(+)}$. This variance exceeds the ideal value of 1, mainly because of the deleterious effect of the residual entanglement between the atomic spin and the light leaving the cavity[49] (Supplementary Information).

Having completed the time-reversal calibration step, we lower the entangling light intensity by 40% to the level for which the metrological gain is expected to peak. To reduce the impact of clock laser noise, we resort to a sequential differential phase measurement[4,6,7,53–55] by implementing two identical rotary echo GPS sequences on $|\uparrow\rangle \rightarrow |c_\downarrow\rangle$ and $|\downarrow\rangle \rightarrow |c_\uparrow\rangle$ transitions (Methods). These two transitions are separated

by a frequency difference of $\Delta_{\uparrow\downarrow} = 2\pi \times 25.3$ kHz, allowing us to work with Rabi frequency of $\Omega = 2\pi \times 4.55$ kHz with no transition cross-talk (Methods). To minimize the interval between the pulses on the two transitions, we adopt an interleaved interrogation (see the pulse diagram above Fig. 4b–d).

We next characterize the signal enhancement due to entanglement. The red points in Fig. 4b compare the signal S_y/S of the time-reversal sequence with entangled states to the reference signal for the unentangled CSS (grey points) as we sweep the relative optical phase α. We observe an increased slope of −2.5(1) near $\alpha = 0$ in the time-reversal sequence, resulting in an 8.0(3) dB increase in the signal power, compared with the perfect unentangled sequence. We also note that time reversal amplifies the signal power by 10.2(4) dB compared with the CSS reference sequence without squeezing, which features a reduced slope of 0.77(1).

To verify that the observed quantum amplification offers phase sensitivity below the SQL, we also evaluate the spin noise in S_y at the end of the sequence. Figure 4c shows the histogram of S_y/S measured in the presence of squeezing–unsqueezing dynamics around $S_y/S = 0$, and Fig. 4d shows the histogram of S_z/S measured in the absence of squeezing–unsqueezing dynamics around $S_z/S = 0$. The CSS noise features a normalized variance of 1.1(2), consistent with the SQL (Methods). By contrast, the normalized variance measured after the quantum amplification of 3.6(5) visibly exceeds its benchmark counterpart of 2.5(4). This is explained by the amplification of the residual laser noise in the sequence at the level of 10% of the SQL.

Finally, based on the measured slope and spin noise, we infer a directly measured metrological gain of $\mathcal{G} = (\partial_\phi S_y)^2/[2S(\Delta S_y)^2] = 2.4(7)$ dB below the SQL and 4.0(8) dB with the laser noise subtracted. We stress that because our measurement realizes a comparison of two optical frequencies, the characterized level of performance of 4.0(8) dB directly translates to the improved measurement precision of the frequency of the clock LO laser relative to a single clock transition (Fig. 2). Our experiment constitutes another direct measurement of sub-SQL phase sensitivity on an optical clock transition, following the previous demonstrations using spin squeezing mapping[37] and Rydberg-generated GHZ states of four atoms[12]. However, we highlight that the method demonstrated here offers superior scalability to much larger systems, owing to the intrinsically all-to-all character of the entangling interaction. For the current experimental cycle time of 5 s, we infer a frequency instability of $2.0 \times 10^{-13}/\sqrt{\tau}$ for the differential phase measurement. Promising routes to further improvement include implementing a GPS sequence with lower Rabi frequency to extend the phase interrogation time, reducing the dead time through reusing the atoms multiple times after cavity non-destructive measurement and improving the LO performance itself.

In conclusion, we have demonstrated the first, to our knowledge, quantum amplification of the phase encoded on an optical clock transition and directly observed sensitivity below the SQL. We have achieved this while developing a spectroscopic method that uses the concepts of holonomic quantum gates[18], measuring the frequency-dependent global phase of the two-level clock system with reference to a third level. Importantly, this has allowed us to extend entanglement-enhanced metrology to Rabi-type spectroscopy (entanglement-enhanced measurement of the Rabi drive amplitude has been demonstrated in ref. 34). We have also identified the rotary echo in Rabi spectroscopy as a practical tool to suppress inhomogeneous broadening, enabling composite precision spectroscopy. In the future, we anticipate achieving further increased metrological gain by using non-Gaussian probe states involving more atoms. Based on our previous work[47], the improvements should follow the Heisenberg scaling. The phase amplification technique on the clock transition can also be extended to multiple ensembles, opening avenues for quantum-enhanced multiplexed optical lattice clocks[7], optical clock networks[56], multi-parameter estimation[57], distributed sensing techniques[58] and protocols balancing the gain–bandwidth trade-off[21]. We also expect our method of differential measurement to be readily applicable to the search for new physics, such as Lorentz symmetry violation[59].

Online content

Any methods, additional references, Nature Portfolio reporting summaries, source data, extended data, supplementary information, acknowledgements, peer review information; details of author contributions and competing interests; and statements of data and code availability are available at https://doi.org/10.1038/s41586-025-09578-8.

1. Ludlow, A. D., Boyd, M. M., Ye, J., Peik, E. & Schmidt, P. O. Optical atomic clocks. *Rev. Mod. Phys.* **87**, 637–701 (2015).
2. Ushijima, I., Takamoto, M., Das, M., Ohkubo, T. & Katori, H. Cryogenic optical lattice clocks. *Nat. Photon.* **9**, 185–189 (2015).
3. Oelker, E. et al. Demonstration of 4.8×10^{-17} stability at 1s for two independent optical clocks. *Nat. Photon.* **13**, 714–719 (2019).
4. Schioppo, M. et al. Ultrastable optical clock with two cold-atom ensembles. *Nat. Photon.* **11**, 48–52 (2017).
5. Li, J. et al. A strontium lattice clock with both stability and uncertainty below 5×10^{-18}. *Metrologia* **61**, 015006 (2024).
6. Robinson, J. M. et al. Direct comparison of two spin-squeezed optical clock ensembles at the 10^{-17} level. *Nat. Phys.* **20**, 208–213 (2024).
7. Zheng, X. et al. Differential clock comparisons with a multiplexed optical lattice clock. *Nature* **602**, 425–430 (2022).
8. Pezzè, L., Smerzi, A., Oberthaler, M. K., Schmied, R. & Treutlein, P. Quantum metrology with nonclassical states of atomic ensembles. *Rev. Mod. Phys.* **90**, 035005 (2018).
9. Monz, T. et al. 14-qubit entanglement: creation and coherence. *Phys. Rev. Lett.* **106**, 130506 (2011).
10. Pogorelov, I. et al. Compact ion-trap quantum computing demonstrator. *PRX Quantum* **2**, 020343 (2021).
11. Leibfried, D. et al. Creation of a six-atom 'Schrödinger cat' state. *Nature* **438**, 639–642 (2005).
12. Cao, A. et al. Multi-qubit gates and Schrödinger cat states in an optical clock. *Nature* **634**, 315–320 (2024).
13. Kitagawa, M. & Ueda, M. Squeezed spin states. *Phys. Rev. A* **47**, 5138–5143 (1993).
14. Yurke, B., McCall, S. L. & Klauder, J. R. SU(2) and SU(1,1) interferometers. *Phys. Rev. A* **33**, 4033–4054 (1986).
15. Wineland, D. J., Bollinger, J. J., Itano, W. M. & Heinzen, D. J. Squeezed atomic states and projection noise in spectroscopy. *Phys. Rev. A* **50**, 67–88 (1994).
16. Davis, E., Bentsen, G. & Schleier-Smith, M. Approaching the Heisenberg limit without single-particle detection. *Phys. Rev. Lett.* **116**, 053601 (2016).
17. Fröwis, F., Sekatski, P. & Dür, W. Detecting large quantum Fisher information with finite measurement precision. *Phys. Rev. Lett.* **116**, 090801 (2016).
18. Sjöqvist, E. Nonadiabatic holonomic single-qubit gates in off-resonant Λ systems. *Phys. Lett. A* **380**, 65–67 (2016).
19. Aharonov, Y. & Anandan, J. Phase change during a cyclic quantum evolution. *Phys. Rev. Lett.* **58**, 1593–1596 (1987).
20. Kaubruegger, R., Vasilyev, D. V., Schulte, M., Hammerer, K. & Zoller, P. Quantum variational optimization of Ramsey interferometry and atomic clocks. *Phys. Rev. X* **11**, 041045 (2021).
21. Liu, Q. et al. Enhancing dynamic range of sub-standard-quantum-limit measurements via quantum deamplification. *Phys. Rev. Lett.* **135**, 040801 (2025).
22. Marciniak, C. D. et al. Optimal metrology with programmable quantum sensors. *Nature* **603**, 604–609 (2022).
23. Mehlstäubler, T. E., Grosche, G., Lisdat, C., Schmidt, P. O. & Denker, H. Atomic clocks for geodesy. *Rep. Prog. Phys.* **81**, 064401 (2018).
24. Safronova, M. S. et al. Search for new physics with atoms and molecules. *Rev. Mod. Phys.* **90**, 025008 (2018).
25. Kolkowitz, S. et al. Gravitational wave detection with optical lattice atomic clocks. *Phys. Rev. D* **94**, 124043 (2016).
26. Sanner, C. et al. Optical clock comparison for Lorentz symmetry testing. *Nature* **567**, 204–208 (2019).
27. Wcisło, P. et al. New bounds on dark matter coupling from a global network of optical atomic clocks. *Sci. Adv.* **4**, eaau4869 (2018).
28. Song, C. et al. Generation of multicomponent atomic Schrödinger cat states of up to 20 qubits. *Science* **365**, 574–577 (2019).
29. Omran, A. et al. Generation and manipulation of Schrödinger cat states in Rydberg atom arrays. *Science* **365**, 570–574 (2019).
30. Finkelstein, R. et al. Universal quantum operations and ancilla-based read-out for tweezer clocks. *Nature* **634**, 321–327 (2024).
31. Gross, C., Zibold, T., Nicklas, E., Estève, J. & Oberthaler, M. K. Nonlinear atom interferometer surpasses classical precision limit. *Nature* **464**, 1165–1169 (2010).
32. Riedel, M. F. et al. Atom-chip-based generation of entanglement for quantum metrology. *Nature* **464**, 1170–1173 (2010).
33. Hosten, O., Engelsen, N. J., Krishnakumar, R. & Kasevich, M. A. Measurement noise 100 times lower than the quantum-projection limit using entangled atoms. *Nature* **529**, 505–508 (2016).
34. Bao, H. et al. Spin squeezing of 10^{11} atoms by prediction and retrodiction measurements. *Nature* **581**, 159–163 (2020).
35. Anders, F. et al. Momentum entanglement for atom interferometry. *Phys. Rev. Lett.* **127**, 140402 (2021).

36. Greve, G. P., Luo, C., Wu, B. & Thompson, J. K. Entanglement-enhanced matter-wave interferometry in a high-finesse cavity. *Nature* **610**, 472–477 (2022).
37. Pedrozo-Peñafiel, E. et al. Entanglement on an optical atomic-clock transition. *Nature* **588**, 414–418 (2020).
38. Sewell, R. J. et al. Magnetic sensitivity beyond the projection noise limit by spin squeezing. *Phys. Rev. Lett.* **109**, 253605 (2012).
39. Muessel, W., Strobel, H., Linnemann, D., Hume, D. B. & Oberthaler, M. K. Scalable spin squeezing for quantum-enhanced magnetometry with Bose-Einstein condensates. *Phys. Rev. Lett.* **113**, 103004 (2014).
40. Cassens, C., Meyer-Hoppe, B., Rasel, E. & Klempt, C. Entanglement-enhanced atomic gravimeter. *Phys. Rev. X* **15**, 011029 (2025).
41. Kruse, I. et al. Improvement of an atomic clock using squeezed vacuum. *Phys. Rev. Lett.* **117**, 143004 (2016).
42. Appel, J. et al. Mesoscopic atomic entanglement for precision measurements beyond the standard quantum limit. *Proc. Natl Acad. Sci. USA* **106**, 10960–10965 (2009).
43. Nolan, S. P., Szigeti, S. S. & Haine, S. A. Optimal and robust quantum metrology using interaction-based readouts. *Phys. Rev. Lett.* **119**, 193601 (2017).
44. Hosten, O., Krishnakumar, R., Engelsen, N. J. & Kasevich, M. A. Quantum phase magnification. *Science* **352**, 1552–1555 (2016).
45. Linnemann, D. et al. Quantum-enhanced sensing based on time reversal of nonlinear dynamics. *Phys. Rev. Lett.* **117**, 013001 (2016).
46. Gilmore, K. A. et al. Quantum-enhanced sensing of displacements and electric fields with two-dimensional trapped-ion crystals. *Science* **373**, 673–678 (2021).
47. Colombo, S. et al. Time-reversal-based quantum metrology with many-body entangled states. *Nature Physics* **18**, 925–930 (2022).
48. Schleier-Smith, M. H., Leroux, I. D. & Vuletić, V. Squeezing the collective spin of a dilute atomic ensemble by cavity feedback. *Phys. Rev. A* **81**, 021804 (2010).
49. Braverman, B. et al. Near-unitary spin squeezing in ^{171}Yb. *Phys. Rev. Lett.* **122**, 223203 (2019).
50. Bishof, M., Zhang, X., Martin, M. J. & Ye, J. Optical spectrum analyzer with quantum-limited noise floor. *Phys. Rev. Lett.* **111**, 093604 (2013).
51. Solomon, I. Rotary spin echoes. *Phys. Rev. Lett.* **2**, 301–302 (1959).
52. Blatt, S. et al. Rabi spectroscopy and excitation inhomogeneity in a one-dimensional optical lattice clock. *Phys. Rev. A* **80**, 052703 (2009).
53. Norcia, M. A. et al. Seconds-scale coherence on an optical clock transition in a tweezer array. *Science* **366**, 93–97 (2019).
54. Takamoto, M., Takano, T. & Katori, H. Frequency comparison of optical lattice clocks beyond the Dick limit. *Nat. Photon.* **5**, 288–292 (2011).
55. Nicholson, T. L. et al. Comparison of two independent Sr optical clocks with 1×10^{-17} stability at 10^3 s. *Phys. Rev. Lett.* **109**, 230801 (2012).
56. Riehle, F. Optical clock networks. *Nat. Photon.* **11**, 25–31 (2017).
57. Li, Y. et al. Multiparameter estimation with an array of entangled atomic sensors. Preprint at https://arxiv.org/abs/2504.08677 (2025).
58. Malia, B. K., Wu, Y., Martínez-Rincón, J. & Kasevich, M. A. Distributed quantum sensing with mode-entangled spin-squeezed atomic states. *Nature* **612**, 661–665 (2022).
59. Dzuba, V. A. et al. Strongly enhanced effects of Lorentz symmetry violation in entangled Yb+ ions. *Nat. Phys.* **12**, 465–468 (2016).

Methods

State dynamics during interrogation

Working in the rotating frame of reference, in which the Hamiltonian of the clock laser drive takes the following form:

$$H = \Delta|c_\downarrow\rangle\langle c_\downarrow| + \frac{\Omega}{2}(|c_\downarrow\rangle\langle\uparrow| + |\uparrow\rangle\langle c_\downarrow|), \quad (4)$$

we find the evolution of the initial $\frac{1}{\sqrt{2}}(|\downarrow\rangle + |\uparrow\rangle)$ state to follow equation (1), with

$$\begin{aligned} a_\uparrow(\tau) &= \cos\left(\frac{\Omega\tau}{2}\right) + i\sin\left(\frac{\Omega\tau}{2}\right)\frac{\Delta}{\Omega} \\ a_{c_\downarrow}(\tau) &= -i\sin\left(\frac{\Omega\tau}{2}\right)\frac{\Omega}{\Omega}, \end{aligned} \quad (5)$$

where $\Omega = \sqrt{\Omega^2 + \Delta^2}$ represents the generalized Rabi frequency. At $\tau = 2\pi/\omega$, when the optical qubit undergoes a cyclic evolution, $a_{c_\downarrow} = 0$ and $a_\uparrow = -1$, and the information about the detuning, Δ, is fully contained in the global phase of the optical qubit (equation (2)).

Note that the phase is defined modulo 2π, which removes the ambiguity in choosing the encircled area on the Bloch sphere that is identified with twice the global phase. Also, for nonzero α (that is, the relative phase of successive π-pulses, as in Fig. 2), the encoded geometric phase equals half the area enclosed by the unclosed trajectory and the shortest geodesic connecting the initial and final points[60].

In the experiment, we set $\tau = 2\pi/\Omega$, and for $\Delta \neq 0$, the evolution is only approximately cyclic. However, the resulting corrections scale as $(\Delta/\Omega)^2$ and affect the ground-state superposition along the population axis (S_z), whereas the accessed signal is imprinted along the phase axis (S_y).

Plots of the Wigner quasi-probability distributions

The plots in Fig. 1 were prepared for illustrative purposes using the tools in ref. 61.

Cavity measurement of the ground-state populations

We extract the $|\uparrow\rangle$ population from the vacuum Rabi splitting of the cavity mode, as in ref. 47. Repeating this measurement four times, with RF π-rotations in between, gives access to both the $|\uparrow\rangle$ and $|\downarrow\rangle$ populations and allows for the parameter-agnostic readout of S_z, insensitive to the atom loss[49]. The measurement resolution is limited by Raman scattering on the $|\downarrow\rangle \rightarrow |^3P_1, m_F = +\frac{1}{2}\rangle$ transition, which introduces noise in S_z during cavity transmission probing[49]. This sets the limit of 8–9 dB for the maximal amount of resolvable spin squeezing. The quantum amplification protocol can reach higher metrological gains, regardless of this limit[16,47].

Phase control of the clock laser

Controlling the relative phase of subsequent optical π-rotations, α, involves phase shifts of the RF control signal sent to a double-pass acousto-optic modulator (AOM) and introduces technical dead times of 10 μs over which the optical qubit evolves freely. This is negligibly short compared with the timescales of the π-rotations (around 100–400 μs).

Clock drift cancellation

The clock laser frequency drifts together with the length of the ultralow-expansion reference cavity at a constant rate of 0.1 Hz s^{-1}. We remove this drift with a double-pass AOM fed with the control RF signal that is mixed with a slow ramp at the −0.1 Hz s^{-1} rate. We restart the ramp and reset the clock frequency to the atomic transition every 30 min.

Calibration of cavity cooperativity

We calibrate the cavity cooperativity on the $|\uparrow\rangle \rightarrow |e\rangle$ transition, η, using the method from refs. 47,49. This entails measuring the variances in ηS_z for different ηN, with η = constant and N—the atom number—varied through the use of different atom loading times. The red points in Extended Data Fig. 1 represent the variances of binned datasets, corrected for the measurement resolution effects. The slope of the fitted line, $\eta/4$, shows $\eta = 3.2(2)$.

Differential phase measurement

To characterize the metrological gain in the quantum-amplified GPS, we use a differential phase measurement that relies on driving cyclic evolution on both the $|\uparrow\rangle \rightarrow |c_\downarrow\rangle$ and $|\downarrow\rangle \rightarrow |c_\uparrow\rangle$ clock transitions. Immediately after this double interrogation, the atomic state takes the following form:

$$|\psi\rangle = \frac{1}{\sqrt{2}}[e^{i\phi_\downarrow}|\downarrow\rangle + e^{i\phi_\uparrow}|\uparrow\rangle]. \quad (6)$$

The imprinted phases, $\phi_\uparrow$ and $\phi_\downarrow$, follow equation (2) with transition-specific laser detunings, $\Delta_{\uparrow\rightarrow c_\downarrow}$ and $\Delta_{\downarrow\rightarrow c_\uparrow}$, respectively. Between the two interrogations, the clock laser frequency is stepped by a precisely calibrated transition frequency difference, $\Delta_{\uparrow\downarrow} = 2\pi \times 25.33$ kHz, such that the phases $\phi_\uparrow$ and $\phi_\downarrow$ are mostly dictated by the nearly-common-mode clock laser noise. As the temporal separation between the two interrogation steps is kept to the shortest allowed by the Rabi frequency of $\Omega = 2\pi \times 4.2$ kHz, the phases $\phi_\uparrow$ and $\phi_\downarrow$ are strongly correlated, and the relative phase, $\phi_\uparrow - \phi_\downarrow$, becomes insensitive to the shot-to-shot clock laser noise. Nevertheless, it retains sensitivity to the residual laser noise arising from non-simultaneity of the pulses on distinct transitions, as well as all the effects that would alter the $|\uparrow\rangle \rightarrow |c_\downarrow\rangle$ and $|\downarrow\rangle \rightarrow |c_\uparrow\rangle$ transition frequencies differently.

Relation between differential measurement and the laser–atom comparison

An actual clock operation entails a readout of the laser frequency relative to the (more stable) atomic frequency at a sufficiently long atom–laser interrogation time to precisely measure the laser frequency, as also done in this study (Fig. 2). However, this measurement cannot directly prove operation below the SQL (short of having a second, more stable clock system to compare to, or reverting to near-zero interrogation time) because in the comparison of atomic and laser phases we simply observe shot-to-shot laser frequency fluctuations.

This is true of any sub-SQL clock. The atom–laser clock system uses the atoms to measure the laser frequency, or phase, with a resolution beyond the SQL, but the directly observed noise is not the atomic sub-SQL noise, but the laser frequency deviation relative to the atoms that one attempts to correct. The entangled state of the atoms then allows one to correct the laser phase or frequency with a higher resolution than obtainable with an atomic coherent state.

Our differential measurement constitutes a direct comparison of two stable optical frequencies and provides a workaround to experimentally demonstrate sub-SQL performance of the atomic ensembles, removing the laser frequency noise. The multi-shot statistics from Fig. 4 thus reliably characterize the metrological performance of a single-shot laser–atom frequency comparison.

Clock transition cross-talk under the laser drive

We assess the level of cross-talk between the $|\uparrow\rangle \rightarrow |c_\downarrow\rangle$ and $|\downarrow\rangle \rightarrow |c_\uparrow\rangle$ transitions under the laser drive resonant with the former, and conditions close to those of Fig. 4. For the measured transition frequency difference, $\Delta_{\uparrow\downarrow} = 2\pi \times 25.33$ kHz and Rabi frequency of $\Omega = 2\pi \times 4.2$ kHz, the cross-talk is expected to be negligibly low.

We perform the Rabi and rotary echo sequences following initialization to the $|\uparrow\rangle$ and $|\downarrow\rangle$ states and monitor their subsequent population dynamics (Extended Data Fig. 2). We observe no $|\downarrow\rangle$ population change in both sequences across a single resonant oscillation period.

In hypothetical scenarios with larger Rabi frequencies or smaller transition splittings, preventing $|\downarrow\rangle$ population errors can be achieved by tuning the Rabi frequency to satisfy the condition

$$\Omega = \frac{\Delta_{\uparrow\downarrow}}{\sqrt{n^2-1}} \tag{7}$$

for even n.

Ground-state benchmarks of metrological gain

For benchmarking purposes, we study the amplification and spin noise in the absence of the optical phase encoding. The effect of the optically encoded phase, α, is mimicked with the composite RF rotation, as shown in the pulse diagram above Extended Data Fig. 3a.

Using the same parameters of the entangling light as in the experiments behind the Fig. 4b–d, that is, the same detunings and detected entangling photon numbers (55(7) squeezing and 21(5) unsqueezing photons, transmitted through the cavity and collected with about 8% efficiency), we observe a slope of −3.1(2) in the phase amplification measurement (Extended Data Fig. 3a, red points). The signal power is amplified by 11.0(6) dB compared with the CSS reference (Extended Data Fig. 3a, grey points), consistent with the value from the main text within error bars.

Extended Data Fig. 3b,c presents the spin noise measured in the time reversal and CSS reference sequences under the same conditions. The normalized variance in the time-reversal sequence equals 2.5(4), and, notably, it is lower than that from Fig. 4c as the probe state is not exposed to the laser noise. This dataset allows us to benchmark the metrological gain with the laser noise subtracted. The metrological gain in the ground-state manifold is found as $\mathcal{G} = 5.8(9)$ dB.

Contrast loss

To further verify the coherence preservation in the ground-state manifold after quantum-amplified GPS, we perform RF π-rotations around the $S_y\cos\theta - S_x\sin\theta$ axis, and measure S_z/S as a function of the angle θ. The scan shown in Extended Data Fig. 4a corresponds to the CSS reference sequence in Fig. 4, whereas the one in Extended Data Fig. 4b to the quantum-amplified sequence in Fig. 4. The squeezing–unsqueezing dynamics during the quantum-amplified sequence lowers the contrast from 88(1)% to 69(2)% due to single-particle dephasing from Rayleigh scattering of the entangling photons into free space (Supplementary Information).

Data availability

The datasets for the current study are available as the source data. Requests for more materials should be addressed to the corresponding author. Source data are provided with this paper.

Code availability

The codes used for the analysis included in this study are available from the corresponding author upon request.

60. Zhou, Z., Carrasco, S. C., Sanner, C., Malinovsky, V. S. & Folman, R. Geometric phase amplification in a clock interferometer for enhanced metrology. *Sci. Adv.* **11**, eadr6893 (2025).
61. Koczor, B., Zeier, R. & Glaser, S. J. Fast computation of spherical phase-space functions of quantum many-body states. *Phys. Rev. A* **102**, 062421 (2020).

Acknowledgements We thank G. Wang, S. Tsesses and D. Spierings for discussions. This work was supported in part by ONR (grant nos. N00014-23-1-2577 and DURIP N00014-22-1-2304), the Center for Ultracold Atoms, an NSF-funded Frontier Center (grant no. PHY-2317134), the NSF Quantum Leap Challenge Institute Award OMA (grant no. 2016244) and DARPA (grant no. HR00112420357). We also acknowledge the support from the US Department of Energy, Office of Science, the National Quantum Information Science Research Centers and the Quantum Systems Accelerator.

Author contributions L.Z., Q.L. and G.V. carried out the experimental setup upgrades, with help from E.P.-P., and M.R. upgraded the control software. L.Z., Q.L., G.V. and M.R. performed the experiments, simulations and data analysis. Z.L. and S.C. helped with the simulations. V.V. conceived and supervised the experiment. L.Z., Q.L. and V.V. wrote the paper. All authors discussed the experiment implementation and results and contributed to the paper.

Competing interests The authors declare no competing interests.

Additional information

Supplementary information The online version contains supplementary material available at https://doi.org/10.1038/s41586-025-09578-8.

Correspondence and requests for materials should be addressed to Vladan Vuletić.

Peer review information *Nature* thanks the anonymous reviewers for their contribution to the peer review of this work. Peer reviewer reports are available.

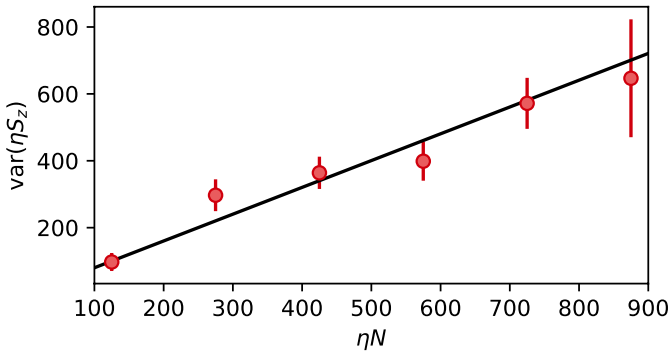

Extended Data Fig. 1 | Calibration of the effective single-atom cavity cooperativity. The red points illustrate the measured variances of ηS_z for binned data sets as a function of the average ηN. The black line is a linear fit with slope of $\eta/4$, yielding $\eta = 3.2(2)$. Numbers of data points per bin (from left to right): 42, 104, 153, 142, 163 and 36. The size of the error bar of the last point results from a lower number of binned data points, and intrinsically larger var(S_z) of the CSS for an increased atom number, N. Error bars indicate 1 s.d.

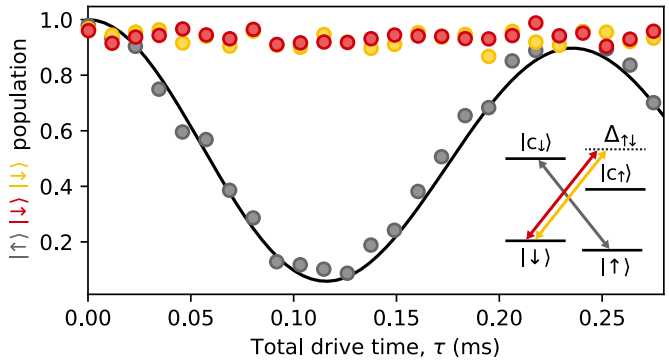

Extended Data Fig. 2 | Evaluation of the transition cross talk. The grey points represent resonant Rabi oscillations on an optical clock transition following initialization to the $|\uparrow\rangle$ state. The red and yellow points correspond to Rabi and rotary echo sequences, respectively, following initialization to the $|\downarrow\rangle$ state. In all three sequences, the laser frequency was resonant with the $|\uparrow\rangle \rightarrow |c_\downarrow\rangle$ transition.

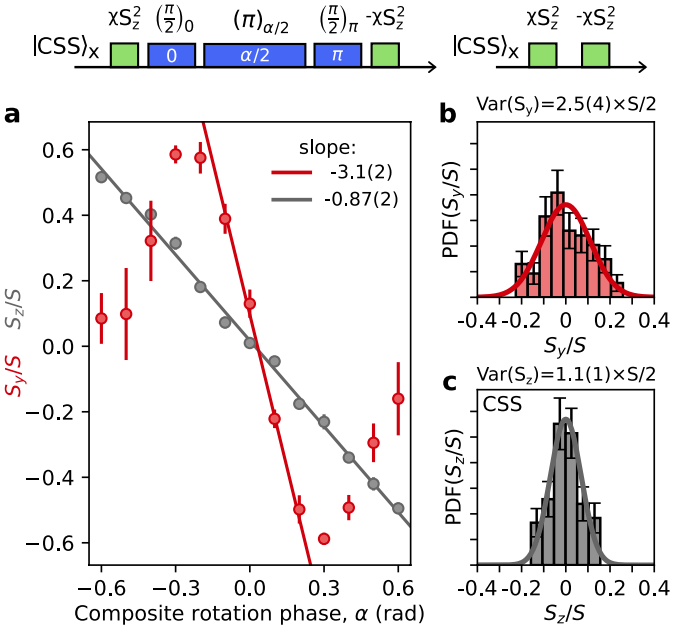

Extended Data Fig. 3 | Metrological gain in the RF phase encoding scheme. **a**, The red (grey) points represent the measured S_y/S (S_z/S) as a function of the composite rotation phase, α, in the time-reversal (CSS reference) sequence. **b**, The spin noise statistics in the time-reversal sequence. **c**, The spin noise statistics in the CSS reference sequence. The 'PDF' in panels **b** and **c** stands for probability density function, estimated based on more than 100 measurement outcomes summarized by the histograms. The color coding in the pulse diagrams is consistent with Fig. 1a-b (Green: entangling light, blue: RF). Error bars indicate 1 s.d.

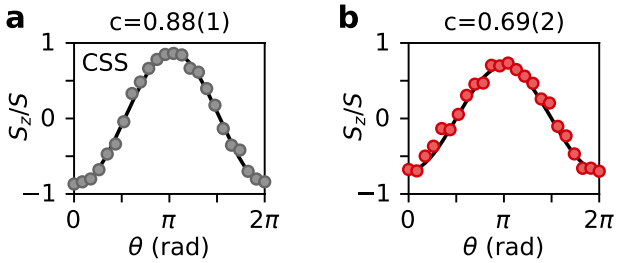

Extended Data Fig. 4 | Contrast loss from Rayleigh scattering during entangling dynamics. a, The contrast measured after the CSS reference sequence from Fig. 4. **b**, The contrast measured after the quantum-amplified sequence from Fig. 4.